THE JOURNAL OF PHYSICAL CHEMISTRY C

Article

pubs.acs.org/JPCC

Atomic Layer Deposition of Lithium Tantalate Solid-State Electrolytes

Jian Liu,[†] Mohammad N. Banis,[†] Xifei Li,[†] Andrew Lushington,[†] Mei Cai,[‡] Ruying Li,[†] Tsun-Kong Sham,[§] and Xueliang Sun*[,†]

[†]Department of Mechanical and Materials Engineering, University of Western Ontario, London, ON, Canada N6A 5B9

[‡]General Motors R&D Center, Warren, Michigan 48090-9055, United States

[§]Department of Chemistry, University of Western Ontario, London, ON, Canada N6A 5B7

Supporting Information

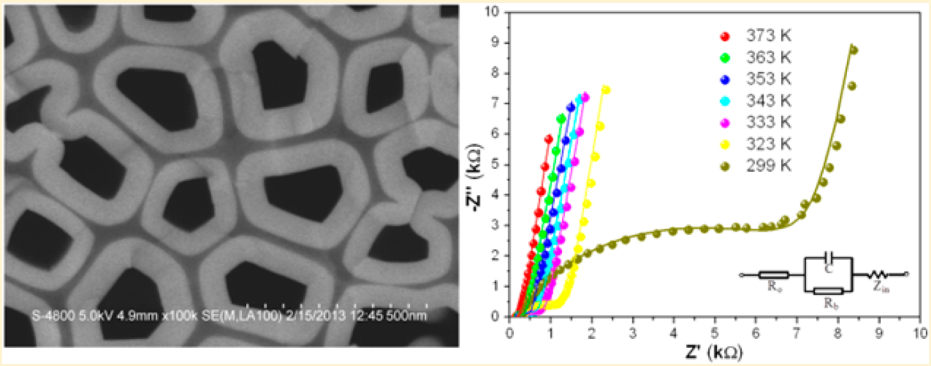

ABSTRACT: 3D all-solid-state microbatteries are promising onboard power systems for autonomous devices. The fabrication of 3D microbatteries needs deposition of active materials, especially solid-state electrolytes, as conformal and pinhole free thin films in 3D architectures, which has proven very difficult for conventional deposition techniques, such as chemical vapor deposition and physical vapor deposition. Herein, we report an alternative technique, atomic layer deposition (ALD), for achieving ideal solid-state electrolyte thin films for 3D microbatteries. Lithium tantalate solid-state electrolytes, with well-controlled film composition and film thickness, were grown by ALD at 225 °C using subcycle combination of $1 \times Li_2O + n \times Ta_2O_5$ ($1 \leq n \leq 10$). The film composition was tunable by varying Ta_2O_5 subcycles (n), whereas the film thickness displayed a linear relationship with ALD cycle number, due to the self-limiting nature of the ALD process. Furthermore, the lithium tantalate thin films showed excellent uniformity and conformity in 3D anodic aluminum oxide template. Moreover, impedance testing showed that the lithium tantalate thin film exhibited a lithium ion conductivity of 2×10^{-8} S/cm at 299 K. The lithium tantalate thin films by ALD, featured with well-controlled film thickness and composition, excellent step coverage, and moderate ionic conductivity at room temperature, would be promising solid-state electrolytes for 3D microbatteries.

1. INTRODUCTION

Microelectronic devices are becoming increasingly incorporated into our daily activities. A great deal of effort has been devoted to developing autonomous devices, such as medical implants, self-powered integrated circuits, and microelectromechanical systems, which need be driven by an on-board power supply system.[1,2] Lithium-ion batteries (LIBs) are a preferable energy medium for these types of applications, due to their ability to deliver high energy density.[2] In particular, all-solid-state LIBs have drawn great attention from various industries, since they can permit greater flexibility in the design of batteries, provide improved intrinsic safety due to the absence of liquid electrolytes, and facilitate miniaturization of microelectronic devices.[1−3] During the past decade, research in the field of all-solid-state LIBs has been primarily focused on two-dimensional (2D) thin film batteries.[4,5] However, it is becoming difficult for 2D thin film batteries to meet the elevated power consumption demand in modern microelectronic devices due to their limited energy density per unit area.[2] One effective strategy to increase the capacity per unit area (μA h cm^{-2}) of all-solid-sate LIBs is developing three-dimensional (3D) microbatteries instead of 2D thin film batteries. 3D microbatteries can offer significantly increased specific surface area of active materials in the same areal footprint as 2D thin film batteries and maintain short path lengths for the diffusion of lithium ion, thereby rendering greatly enhanced battery capacity per unit area.[2,3] Given the advantages and demand of 3D microbatteries, various concepts for their design have been proposed.[1−3,6−9] However, it is still challenging to fabricate real 3D microbatteries, partly due to the great limitations of conventional deposition techniques

Received: June 26, 2013
Revised: September 5, 2013
Published: September 6, 2013

   dx.doi.org/10.1021/jp4063302 | J. Phys. Chem. C 2013, 117, 20260−20267

employed in the fabrication of 2D thin film batteries, such as physical vapor deposition (PVD), chemical vapor deposition (CVD), and electrochemical deposition. One of the most difficult, but crucial, steps in the fabrication of 3D microbatteries is the deposition of conformal and pinhole-free thin films onto 3D structures. The thin films required in 3D microbatteries must be perfect and free of cracks or pinholes, which will result in short circuits and failure of batteries. It has been realized that the key to achieving as-desired thin films in 3D architectures is the use of a deposition technique that is inherently self-limiting.[8,10]

Atomic layer deposition (ALD) has been known as a thin film technique being capable of depositing high-quality films in 3D structures.[11] Unlike other film deposition methods, such as PVD or CVD, ALD employs self-limiting surface reactions via alternating, saturated precursor doses.[12,13] As a consequence, ALD provides exquisite control over the thickness of thin films, and the thin films deposited by ALD have excellent conformality and uniformity, even in 3D substrates with aspect ratio in excess of 1000.[14] These unique features make ALD a suitable technique for fabricating 3D microbatteries, and its potential has been demonstrated recently.[15−17] For example, anatase TiO_2 thin film with 17 nm thickness was deposited by ALD directly on aligned aluminum nanorods, which served as current collectors.[15] The 3D TiO_2 nanoelectrode exhibited a capacity 10 times higher than traditional 2D TiO_2 electrode in the same areal footprint and showed excellent rate capability and stability in 50 charge−discharge cycling. V_2O_5 thin films were deposited using ALD on micropillars coated with TMV/Ni, forming hierarchical 3D electrodes.[17] The conformal V_2O_5 thin films on the 3D micropillar electrodes enabled much higher energy density and faster charge−discharge rate than those on a planar substrate. Even though no real 3D microbatteries have been manufactured by ALD, given the aforementioned exclusive advantages, it is expected that ALD will play an important role in fabricating 3D microbatteries in the near future.

In recent years, ALD has been widely applied in conventional LIBs, either to directly prepare active materials (such as SnO_2, $Li_4Ti_5O_{12}$, V_2O_5)[18−22] or to coat the anode or cathode electrodes with metal oxides (such as Al_2O_3, ZrO_2, ZnO) aiming at improving their performance.[23−32] However, the application of ALD technique in 3D microbatteries is still rare. Advancement in the field of 3D microbatteries prepared by ALD is highly reliant on the development of battery materials, i.e., anodes, solid-state electrolytes, and cathodes.[33,34] Some ALD-derived materials (mainly metal oxide such as TiO_2, SnO_2, V_2O_5) have been directly adopted as anodes or cathodes in 3D microbatteries.[33,34] However, there have been very few reports on the synthesis of solid-state electrolytes by ALD.[35−41] It was not until 2009 that research relevant to solid-state electrolytes deposited by ALD started to emerge, when the ALD process for Li_2O was first investigated.[35] Aaltonen et al.[36] applied ALD to grow lithium lanthanum titanate (LLT) electrolytes at 225 °C by combining subcycles of TiO_2 ($TiCl_4$−H_2O), La_2O_3 ($La(thd)_3$−O_3), and Li_2O (LiO^tBu−H_2O). The LLT thin film deposited at saturation conditions had a composition of $Li_{0.32}La_{0.30}TiO_z$, with amorphous structure. The LLT thin film was crystallized after annealing at 800 °C in oxygen for 3 h. Later on, Li_2O−Al_2O_3 thin films were fabricated by the same group using ALD of Li_2O (LiO^tBu−H_2O) and Al_2O_3 (TMA−O_3).[37] The thickness of the Li_2O−Al_2O_3 thin film was found to depend on ALD cycles linearly, yielding a growth rate of 2.8 Å/cycle. Hämäläinen et al.[38,39] described the deposition of lithium phosphate and lithium silicate thin films by ALD. The lithium phosphate was deposited between 225 and 350 °C using trimethyl phosphate and either of LiHMDS or LiO^tBu, and the lithium silicate was grown in a temperature range of 150−400 °C from LiHMDS and O_3. In both cases, the growth rate and composition of the thin films were dependent on deposition temperature. Furthermore, Li_3N was deposited by ALD from LiHMDS and NH_3 at 167 °C, showing a growth rate of 0.95 Å/cycle.[40] Even though progress on ALD synthesis of solid-state electrolytes has been made, investigation on their lithium-ion conductivity was seldom conducted. Only Aaltonen et al.[37] presented a lithium-ion conductivity of 1×10^{-7} S/cm (at 300 °C) for Li_2O−Al_2O_3 thin film, which had been annealed at 700 °C for 5 h. Unfortunately, the high operating temperature and postannealing requirement seriously hinder application of the Li_2O−Al_2O_3 thin film. The postannealing process increases the risk of cracking in solid-state electrolytes, leading to short circuits and failure of 3D microbatteries. Therefore, it is essential that the solid-state electrolyte thin films are prepared in a "gentle" manner to avoid cracking.

To fulfill the objective above, lithium tantalate was selected as the solid-state electrolyte to be deposited by ALD in this work. Lithium tantalate has the following advantages: (1) Being lithium-ion conductive with amorphous structure. Previous work has found that amorphous phase of lithium tantalate rather than crystalline one was conductive of lithium ions.[42,43] The ALD-deposited lithium tantalate would show a disordered structure due to the low deposition temperature (225 °C) used herein.[35−39] It was expected that the lithium tantalate grown by ALD could be a lithium-ion conductor at the as-deposited condition, saving post-treatment process and avoiding possible cracking of thin films during this process. (2) Displaying acceptable lithium-ion conductivity (10^{-5}−10^{-8} S/cm). (3) Negligible electronic conductivity at room temperature.[42,43] In summary, this work realized the deposition of lithium tantalate thin films by ALD technique, for the first time. The synthesized lithium tantalate thin films were featured with not only precisely controlled film thickness, but well-tuned film composition. Most importantly, the lithium tantalate thin films by ALD, at the as-deposited state, exhibited moderate lithium-ion conductivity at room temperature, with no requirement of further treatments. Furthermore, the ALD approach reported herein could achieve uniform and conformal lithium tantalate thin films in a 3D architecture. It is believed that the lithium tantalate thin films deposited by ALD would have great potential as solid-state electrolytes in 3D microbatteries.

2. EXPERIMENTAL SECTION

All lithium tantalate thin films were deposited at 225 °C in a Savannah 100 ALD system (Cambridge Nanotech Inc.) by combining ALD subcycles of Li_2O and Ta_2O_5. The Li_2O subcycle consisted of alternating pulses of lithium *tert*-butoxide (LiO^tBu, $(CH_3)_3COLi$) and H_2O, while the Ta_2O_5 subcycle consisted of alternating pulses of tantalum(V) ethoxide ($Ta(OEt)_5$, $Ta(OC_2H_5)_5$) and H_2O. The source temperatures for LiO^tBu, $Ta(OEt)_5$, and H_2O were 170, 190, and 23 °C, respectively. The system pipelines were heated to 190 °C in order to prevent condensation of the precursors. The pulse times of LiO^tBu and $Ta(OEt)_5$ were varied from 0.2 to 1.5 s, while the pulse time of H_2O remained at 1 s. All precursor pulses were separated by a 10 s nitrogen purge. One ALD cycle

dx.doi.org/10.1021/jp4063302 | J. Phys. Chem. C 2013, 117, 20260−20267

was executed using a pulsing sequence of 1 × [LiO^{t}Bu (0.2−1.5 s)−purge (10 s)−H_2O (1 s)−purge (10 s)]-n × [$Ta(OEt)_5$ (0.2−1.5 s)−purge (10 s)−H_2O (1 s)−purge (10 s)], which was expressed as 1 × Li_2O + n × Ta_2O_5 ($1 \le n \le 10$) in brief. All lithium tantalate thin films were deposited on planar Si (100) and glass substrates. Anodic aluminum oxide (AAO, Anodisc 13, Whatman) template with aspect ratio of ~300 was chosen as a 3D substrate. All characterizations were carried out on the Si (100) substrate except otherwise noted.

After ALD coatings, the Si (100) substrate was cut into small pieces. One piece of Si (100) with fresh surface was chosen and pasted onto a vertical SEM holder using carbon slurry. The thicknesses of the lithium tantalate thin films were measured from the fresh cross sections of the Si (100) using field-emission scanning electron microscopy (SEM, Hitachi-4800). The thicknesses of the thin films were obtained by taking average of 10 values measured at different locations of each sample. The compositions of the lithium tantalate thin films were analyzed by using X-ray photoelectron spectroscopy (XPS) using Kratos Axis Ultra Al (alpha) spectrometer. The phases of the lithium tantalate thin films on the glass substrate were identified using micro-X-ray diffraction (XRD, Bruker D8, Co Kα source, λ = 1.7892 Å). The Ta L_3 edge X-ray absorption near-edge structure (XANES) measurements were performed on the 06ID superconducting wiggler hard X-ray microanalysis (HXMA) beamline at the Canadian Light Source (CLS) with a premirror−double crystal monochromator−postmirror configuration using Si (111) crystals and Rh mirrors. CLS operates at 2.9 GeV with 175 mA injection current and the beamline wiggler was running at 1.5 T. Measurements were made at room temperature in transmission mode for Ta foil with ion chambers filled with 100% of N_2 and in fluorescence mode for the lithium tantalate thin films using a 32-element Ge detector.

To prepare the sample for impedance testing, ~50 nm Au layer was first sputtered on the glass substrate in a Polaron sputtering system under 2 kV for 9 min, and then the lithium tantalate thin film was deposited on top of the Au layer using a pulsing sequence of 400 × (1 × Li_2O + 6 × Ta_2O_5). Following the ALD deposition, the as-prepared sample was immediately transferred into the Polaron sputtering system for coating of another Au layer (~50 nm in thickness). The thickness of the lithium tantalate thin film (or the distance between the two Au layers) was measured to be ~200 nm, and the area of lithium tantalate thin film was 5 mm × 5 mm. The impedance spectra at different temperatures were obtained by applying 50 mV in a frequency range of 200 kHz−10 Hz on a CHI electrochemistry workstation. The sample was left to stabilize at each temperature for 30 min before acquiring data.

3. RESULTS AND DISCUSSION

Figures 1a and 1b show the effect of LiO^{t}Bu and $Ta(OEt)_5$ pulse times on the growth per cycle (GPC) of the lithium tantalate system deposited using a pulsing sequence of (1 × Li_2O + 1 × Ta_2O_5). It can be seen that the GPC stabilizes at around 2.1 Å/cycle, when pulse times for $Ta(OEt)_5$ and LiO^{t}Bu are longer than 0.5 and 1 s, respectively. Thus, $Ta(OEt)_5$ and LiO^{t}Bu pulse lengths of 0.5 and 1 s, respectively, are sufficient to achieve saturated growth of the lithium tantalate thin film, and are chosen to be employed in subsequent experiments.

The lithium tantalate thin films are deposited using pulsing sequences of 1 × Li_2O + n × Ta_2O_5 (n = 1, 6, and 10), where subcycle number of Ta_2O_5 (n) is varied in order to change film composition (Li/Ta ratio). The morphologies of the as-deposited thin films are examined by SEM. Figure 2 displays the result of the lithium tantalate thin film deposited using a pulsing sequence of 1 × Li_2O + 6 × Ta_2O_5 as an example. From top-view observation in Figure 2a, it can be seen that 400-cycle lithium tantalate thin film is uniformly coated on the whole Si substrate, with a slight roughness associated with the film surface (Figure 2b). Cross-sectional views in Figure 2c clearly show the thicknesses of the lithium tantalate thin films deposited with different ALD cycles (low-magnification images included in Figure SI-1 of the Supporting Information). The thickness measurements by SEM are plotted as a function of ALD cycle number in Figure 3. XRD analysis (Figure SI-2) reveals amorphous structure of the as-grown lithium tantalate thin films.

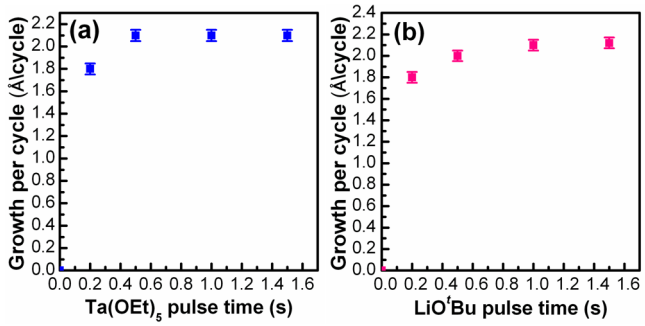

Figure 1. Growth per cycle of the lithium tantalate thin film as a function of (a) $Ta(OEt)_5$ pulse time and (b) LiO^{t}Bu pulse time using a pulsing sequence of 400 × (1 × Li_2O + 1 × Ta_2O_5).

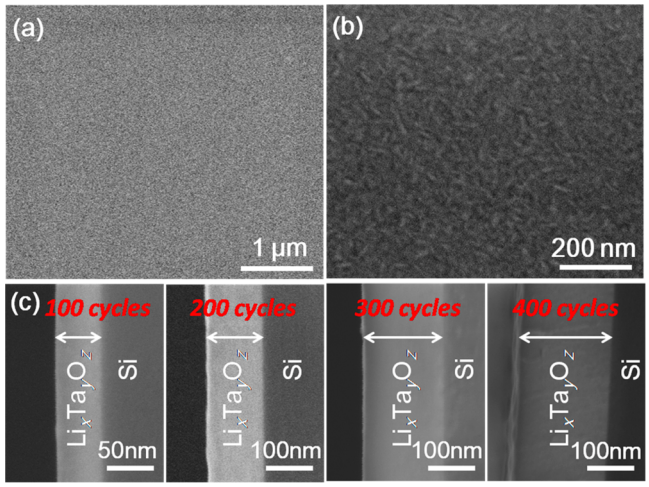

Figure 2. SEM morphology of lithium tantalate thin film deposited using a pulsing sequence of (1 × Li_2O + 6 × Ta_2O_5): (a, b) top view of 400-cycle thin film and (c) cross-section views of the thin films deposited with different ALD cycles.

Figure 3a shows the ALD-cycle dependence of lithium tantalate film thickness when different pulsing sequences are employed. It is clear that the lithium tantalate film thickness is linearly dependent with ALD cycle, demonstrating the self-limiting behavior during the ALD process. By fitting the data in Figure 3a linearly, the GPC of the lithium tantalate thin film is calculated to be 2.2, 5.2, and 7.3 Å/cycle, where n equals to 1, 6, and 10, respectively, in one (1 × Li_2O + n × Ta_2O_5) cycle (as plotted in Figure 3b). From Figure 3b, one can see that the GPC of the lithium tantalate thin films increases monotonously

dx.doi.org/10.1021/jp4063302 | J. Phys. Chem. C 2013, 117, 20260−20267

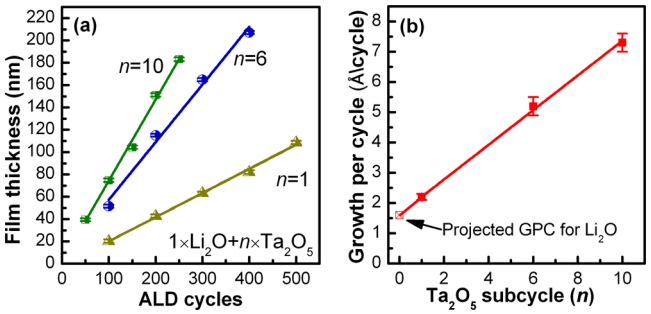

Figure 3. (a) Thickness of the lithium tantalate thin films as a function of ALD cycle number and (b) the growth per cycle of the lithium tantalate thin films as a function of Ta_2O_5 subcycle number, using pulsing sequences of 1 × Li_2O + n × Ta_2O_5 (n = 1, 6, and 10).

with Ta_2O_5 subcycle number (n) in one complete ALD cycle (1 × Li_2O + n × Ta_2O_5). This trend indicates that the GPC of the lithium tantalate thin films is a linear combination of the GPC of the Li_2O subcycle and Ta_2O_5 subcycle. Thereby, two parameters could be extracted from the best-linear-fit in Figure 3b: the slope represents the GPC of the Ta_2O_5 subcycle (~0.5 Å/cycle), while the y-axis intercept of the linear fit represents the GPC of solely the Li_2O subcycle (~1.7 Å/cycle). The GPC of the Li_2O and Ta_2O_5 subcycles obtained herein have good agreement with reported valves of Li_2O at 1.7 Å/cycle[37] and Ta_2O_5 at 0.4 Å/cycle.[44] A better understanding of the ALD process can be derived from looking at the reaction mechanism for each subcycle. As proposed by Aaltonen et al.,[37] during the Li_2O subcycle, the LiO^tBu pulse leads to the formation of two layers, resulting in a high GPC of the Li_2O subcycle:

$$-OH^* + LiOC(CH_3)_3 \rightarrow -O-Li^* + HOC(CH_3)_3 \quad (1)$$

$$-O-Li^* + LiOC(CH_3)_3 \rightarrow -O(-Li)-LiOC(CH_3)_3^* \quad (2)$$

where an asterisk denotes surface species. During the water pulse, the surface species generated in eq 2 are converted to hydroxide groups:[37,45]

$$-O(-Li)-LiOC(CH_3)_3^* + H_2O \rightarrow -O(-Li)-LiOH^* + HOC(CH_3)_3 \quad (3)$$

During the Ta_2O_5 subcycle, the following surface reaction occurs:[46]

$$n(-OH)^* + Ta(OC_2H_5)_5 \rightarrow (-O-)_nTa(OC_2H_5)_{5-n}^* + nHOC_2H_5 \quad (4)$$

$$(-O-)_nTa(OC_2H_5)_{5-n}^* + (5-n)H_2O \rightarrow (-O-)_nTa(OH)_{5-n}^* + (5-n)HOC_2H_5 \quad (5)$$

Therefore, the surface reactions during one complete (1 × Li_2O + n × Ta_2O_5) cycle would occur in the following sequence:

$$\text{Equations (1)(2)} \rightarrow (3) \rightarrow \overset{n}{(4)} \rightarrow (5)$$

One can find that the film surfaces after Li_2O and Ta_2O_5 subcycles are terminated with the same functional groups (−OH). Thus, the surface species available after each Li_2O subcycle are readily reactive sites for the succeeding Ta_2O_5 subcycle, and vice versa. This condition ensures that the Li_2O and Ta_2O_5 subcycles in the combined ALD process proceed in the same manner as in each binary oxide, therefore leading to the similar GPC of Li_2O and Ta_2O_5 in the ternary system as in each binary system. The self-limiting characteristic of the Li_2O and Ta_2O_5 subcycles takes responsibility for the linear relationship between the lithium tantalate film thickness and ALD cycles (Figure 3a) and between the GPC of the lithium tantalate films on Ta_2O_5 subcycle number (Figure 3b). It is worth mentioning that in a ternary or quaternary system deposited by ALD, the GPC of the combined oxide processes is usually lower than what is expected from a linear combination of the GPC of each binary oxide.[36,47] For example, the average GPC of La−Ti−O films grown by combining La_2O_3 and TiO_2 subcycles was found to be below the theoretical GPC calculated from individual growth rate of La_2O_3 (0.28 Å/cycle) and TiO_2 (0.52 Å/cycle).[36] The reason was most likely due to the difference in the surface chemistry between the preceding and the succeeding subcycles, which could alter the GPC of one or each binary system when they are combined. This difference was more obvious in the Li−La−Ti−O system, which was fabricated using Li_2O, La_2O_3, and TiO_2 subcycles. It was found that the pulsing order of the three subcycles had a substantial influence on the Li−La−Ti−O films. The film grown by using a sequence of TiO_2−La_2O_3−Li_2O was less rough and more uniform than that deposited using a TiO_2−Li_2O−La_2O_3 pulsing sequence.[36] Thus, precursor combination and pulsing sequence should be carefully selected when depositing thin films composed of two or more ALD subcycles. From the calculation in Figure 3b, one can find that the GPC of the Ta_2O_5 subcycle (~0.5 Å/cycle) is slightly higher than that of binary Ta_2O_5 (0.4 Å/cycle) reported in the literature.[44] The higher GPC of Ta_2O_5 in our case might be due to denser regeneration of hydroxide groups after each Li_2O subcycle (eq 3) than those produced after each Ta_2O_5 subcycle (eq 5). Another reason that cannot be excluded is the possibility of physisorbed water remaining on the surface after reaction 3 and/or reaction 5. Physisorbed water may lead to CVD-like growth of thin film during the $Ta(OEt)_5$ pulse, thus leading to a higher GPC of Ta_2O_5 than expected.

The structure of amorphous materials is difficult to determine by diffraction-based techniques due to the lack of long-range order. By contrast, X-ray spectroscopy is sensitive to the local environment of the element to be examined and thus is ideal and powerful for analyzing amorphous materials.[48] By comparing the X-ray spectra of unknown and reference materials, it is possible to gain insight into the structure of noncrystalline materials.[48,49] Thus, XANES and XPS techniques were employed to study the structure or/and composition of the amorphous lithium tantalate thin films deposited by ALD in this work. Figure 4 displays XANES at Ta L_3 edge for the lithium tantalate thin films, in comparison with reference crystalline $LiTaO_3$ and pure Ta. The peak at the L_3 edge arises from Ta $2p_{3/2}$ to unoccupied Ta 5d states via dipole transition, and its intensity is expected to be higher in $LiTaO_3$ and exhibits a blue shift since Ta is in a higher oxidation state (d charge depletion). In Figure 4, it can be seen that all the lithium tantalate thin films have very similar Ta L_3-edge spectrum to reference $LiTaO_3$, except that the lithium tantalate thin films exhibit one broad peak at ~9886.5 eV, instead of two well-resolved peaks at 9884.5 and 9886.8 eV for reference crystalline $LiTaO_3$.[50] This slight difference is attributable to the amorphous state of the lithium tantalate thin films.[51,52] In Figure 4, it is also obvious that the Ta L_3-edge XANES of the lithium tantalate thin films are remarkably different from that of

dx.doi.org/10.1021/jp4063302 | J. Phys. Chem. C 2013, 117, 20260−20267

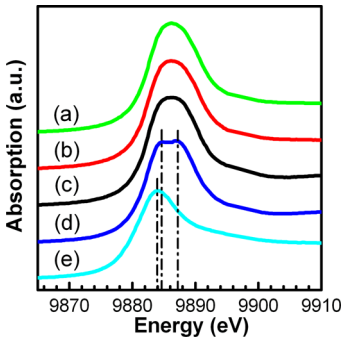

Figure 4. Ta L_3-edge XANES spectra of lithium tantalate thin films deposited using pulsing sequences of $1 \times Li_2O + n \times Ta_2O_5$ where (a) $n = 1$, (b) $n = 6$, and (c) $n = 10$, (d) reference crystalline $LiTaO_3$, and (e) pure Ta.

pure Ta metal as expected. The XANES result indicates that the Ta in lithium tantalate thin films have similar chemical binding (Li−O−Ta) as that in reference $LiTaO_3$ with a noticeable broadening due to disorder.

Compositions of the lithium tantalate thin films were analyzed by XPS, and the results are displayed in Figure 5. The XPS survey in Figure 5a indicates the presence of Li, Ta, and O elements in all the lithium tantalate thin films (their atomic percentages listed in SI-Table 1). The chemical formula is determined as $Li_{12.3}TaO_z$, $Li_{5.1}TaO_z$, and $Li_{0.6}TaO_z$, for the lithium tantalate thin film deposited using a Ta_2O_5 subcycle number of 1, 6, and 10, respectively, while Li_2O was kept constant at 1. XPS data reveal that the Li/Ta ratio of the lithium tantalate thin films decreases with increasing Ta_2O_5 subcycle number, as plotted in Figure 5b. Figure 5c illustrates the chemical environment of Ta element in the lithium tantalate thin films by analyzing the Ta 4f spectrum. For $Li_{12.3}TaO_z$ and $Li_{5.1}TaO_z$, the Ta 4f spectrum is fitted into one set of doublet Ta $4f_{5/2}$ (peak A) and Ta $4f_{7/2}$ (peak B). The positions of Ta $4f_{5/2}$ (peak A) and Ta $4f_{7/2}$ (peak B) are centered at 27.7 and 25.8 eV for $Li_{12.3}TaO_z$ and at 27.9 and 26.0 eV for $Li_{5.1}TaO_z$, respectively. The slight shift of Ta $4f_{5/2}$ (peak A) and Ta $4f_{7/2}$ (peak B) is due to the stoichiometry change from $Li_{12.3}TaO_z$ to $Li_{5.1}TaO_z$. The positions of the Ta $4f_{5/2}$ (peak A) and Ta $4f_{7/2}$ (peak B) are very close to those reported in stoichiometric $LiTaO_3$ film,[53] revealing that the Ta in $Li_{12.3}TaO_z$ and $Li_{5.1}TaO_z$ has a similar chemical binding (Li−O−Ta) as stoichiometric $LiTaO_3$. Deconvolution of Ta 4f peak of $Li_{0.6}TaO_z$ is composed of two pairs of doublets. The one pair of Ta $4f_{5/2}$ (peak A) and Ta $4f_{7/2}$ (peak B) at lower binding energy are consistent with those in $Li_{5.1}TaO_z$. The other pair of Ta $4f_{5/2}$ (peak A′) and Ta $4f_{7/2}$ (peak B′) at higher binding energy are located at 29.2 and 27.3 eV, respectively, which seem similar to the binding energy of Ta in stoichiometric Ta_2O_5.[54] This result indicates that the Ta element in $Li_{0.6}TaO_z$ exists in two types of chemical environments, i.e., Li−O−Ta and Ta−O−Ta, which make up 82% and 18%, respectively. The appearance of Ta−O−Ta obviously resulted from the more Ta_2O_5 subcycles employed during the deposition of $Li_{0.6}TaO_z$. Besides the above elements, carbon is also detected in all thin films prepared (Figure 5a). The presence of carbon can be addressed to organic carbons in C−C, C−H (284.8 eV), C−OH, C−O−C (286.3 eV), O−C=O (288.8 eV), and C=O (287.2 eV) (see Figure SI-3). The source of carbon is a result of ligand residue of ALD precursors as well as hydrocarbons present in ambient air.[55] In $Li_{12.3}TaO_z$, another major source of carbon impurity is carbonate (290.1 eV) (Figure SI-3), which is commonly found in lithium-containing thin films produced by ALD.[37,55] Carbonate present results from a reaction between Li_2O and ambient carbon dioxide when the thin films are exposed to air[45] and thereby should predominantly reside on the topmost surface of the thin film.[37,55] In $Li_{5.1}TaO_z$ and $Li_{0.6}TaO_z$, carbonate only accounts for 4−6% of the carbon impurity compared to 40% in $Li_{12.3}TaO_z$ (Figure SI-3). This difference could be explained by the fact that more Ta_2O_5 subcycles were used in ALD process of $Li_{5.1}TaO_z$ and $Li_{0.6}TaO_z$ than $Li_{12.3}TaO_z$, and resultant thicker Ta_2O_5 layer in the former films can better prevent the reaction of Li_2O with ambient carbon dioxide. $Li_{5.1}TaO_z$ thin film is chosen to be further studied in terms of the lithium-ion conductivity because it is stable in air and easy for operation. More importantly, the excess Li content in $Li_{5.1}TaO_z$ thin film is beneficial for lithium-ion conduction according to previous studies.[53,56]

Lithium-ion conductivity of 400-cycle $Li_{5.1}TaO_z$ thin film (~200 nm thick) was assessed by using electrochemical impedance spectroscopy. Figure 6a shows Cole−Cole plots of the $Li_{5.1}TaO_z$ thin film measured at different temperatures. It can be seen that each Cole−Cole plot consists of one semicircle in the high-frequency region and an inclined tail in the low-frequency region. The former semicircle could be assigned to the bulk resistance of $Li_{5.1}TaO_z$ solid-state electrolyte,[42] while the latter is attributable to the polarization at electrode−electrolyte interface.[57] It is worth noting that the inclined tail in

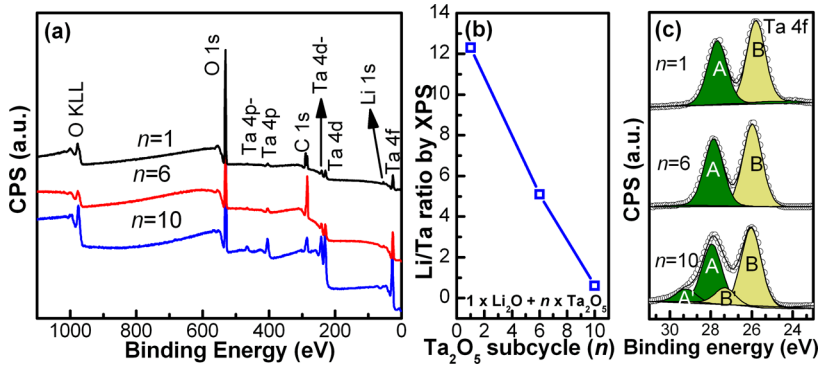

Figure 5. (a) XPS survey of the lithium tantalate thin films deposited using pulsing sequences of $1 \times Li_2O + n \times Ta_2O_5$ ($n = 1$, 6, and 10), (b) Li/Ta ratio in the thin films as a function of Ta_2O_5 subcycle number (n), and (c) deconvolution of Ta 4f spectra. In (c), the components A and A′ correspond to the Ta $4f_{5/2}$ lines, and the components B and B′ correspond to the Ta $4f_{7/2}$ lines.

dx.doi.org/10.1021/jp4063302 | J. Phys. Chem. C 2013, 117, 20260−20267

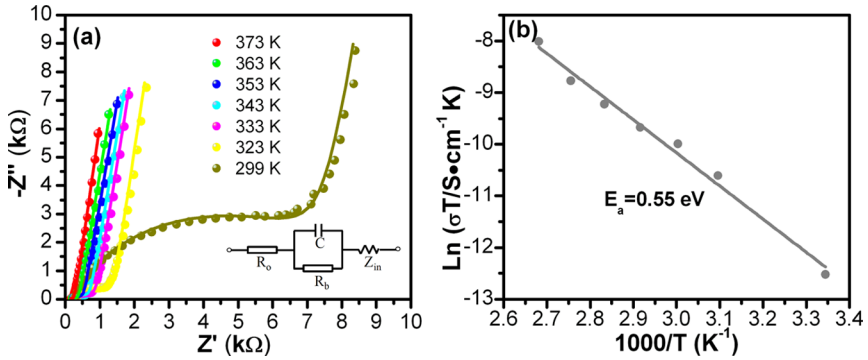

Figure 6. (a) Impedance plots of the $Li_{5.1}TaO_z$ thin film measured at different temperatures (inset shows the equivalent circuit for fitting). (b) Arrhenius plot of the ionic conductivity of the $Li_{5.1}TaO_z$ thin film.

Table 1. Comparisons of Lithium Tantalate and $Li_2O-Al_2O_3$ Solid-State Electrolytes

solid-state electrolyte	substrate type	Li^+ conductivity (S/cm)	activation energy (eV)	preparation method	ref
amorphous Li_xTaO_y	ITO film (planar)	8×10^{-8} (at 300 K)	0.25	RF sputtering	42
$Li_2O-Al_2O_3$	sapphire/Si(111) (planar)	1×10^{-7} (at 573 K)	2.90	ALD	37
amorphous $Li_{5.1}TaO_z$	Si(100)/glass (planar); AAO (3D, aspect ratio ~300)	2×10^{-8} (at 299 K)	0.55	ALD	this work

the case of ionic blocking electrodes (such as Au used herein) is typical indication that the investigated solid-state electrolyte is predominately ionic conductor in nature.[57,58] The Cole–Cole plots could be well-resolved using the equivalent circuit inset in Figure 6a, in which R_b and C represent the bulk resistance and the resultant capacitance of the $Li_{5.1}TaO_z$ solid-state electrolyte, respectively, Z_{in} denotes the polarization impedance of the electrode–electrolyte interface, and R_o is the ohmic resistance of the electrodes.[42] R_b values are obtained in Figure 6a at different temperatures, and the ionic conductivity of the $Li_{5.1}TaO_z$ solid-state electrolyte is derived from the equation[59]

$$\sigma = d/AR_b \quad (6)$$

where σ is the ionic conductivity, d is the thickness of the $Li_{5.1}TaO_z$ film, and A is the area of the $Li_{5.1}TaO_z$ film between Au electrodes. The ionic conductivity of $Li_{5.1}TaO_z$ varies from 1.2×10^{-8} to 9.0×10^{-7} S/cm, at temperatures between 299 and 373 K. Furthermore, variation of the ionic conductivity with temperature is shown in an Arrhenius representation according to[59,60]

$$\sigma T = \sigma_0 \exp[-E_a/(kT)] \quad (7)$$

where E_a denotes the activation energy, k is the Boltzmann constant, T is the absolute temperature, and σ_0 is a constant. Activation energy of ~0.55 eV is obtained by fitting the temperature dependence of the lithium-ion conductivity in Figure 6b. Comparisons are made between $Li_{5.1}TaO_z$, Li_xTaO_y prepared by RF sputtering and $Li_2O-Al_2O_3$ grown by ALD in Table 1. It can be found that the lithium-ion conductivity of $Li_{5.1}TaO_z$ (2×10^{-8} S/cm at 299 K) is comparable with that of amorphous Li_xTaO_y prepared by RF sputtering (8×10^{-8} S/cm at 300 K).[42] For the $Li_2O-Al_2O_3$, its lithium-ion conductivity was estimated to be around 1×10^{-7} S/cm at 573 K, and no data at room temperature was reported.[37] Furthermore, the $Li_2O-Al_2O_3$ exhibits a much higher activation energy (2.9 eV) than $Li_{5.1}TaO_z$ (0.55 eV) and amorphous Li_xTaO_y (0.25 eV). The lithium-ion conductivity of $Li_{5.1}TaO_z$ is considerably low compared with popular solid-state electrolytes (such as NASICON-type, Garnet-type)[61,62] deposited by the PVD method in 2D batteries. However, these popular solid-state electrolytes are not applicable in 3D microbatteries due to the limitation of their preparation method (PVD) in 3D substrates. For applications in 3D microbatteries, the deposition technique should allow uniform coating of solid-state electrolytes in a 3D architecture. $Li_{5.1}TaO_z$ prepared by ALD in our case does meet this requirement for 3D microbatteries, as demonstrated in Figure 7. Moreover, compared with solid-state electrolytes

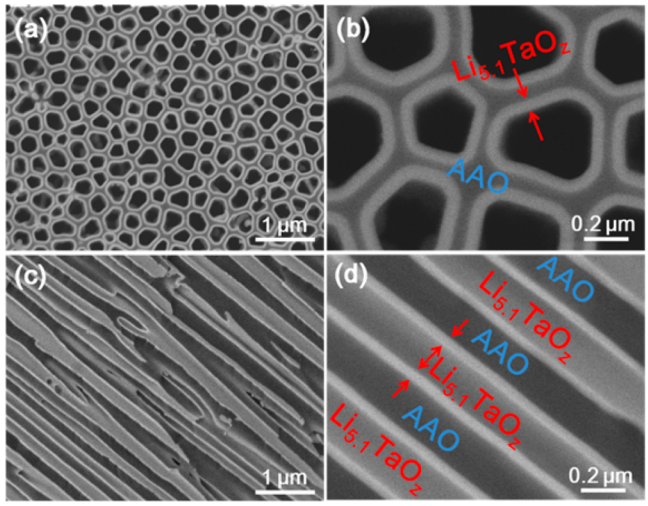

Figure 7. Backscattered electron (BSE) images of 100-cycle $Li_{5.1}TaO_z$ thin film deposited in AAO template: (a, b) top-view and (c, d) cross-section view.

prepared by PVD, ALD-deposited $Li_{5.1}TaO_z$ has much thinner film thickness, which in return can greatly reduce its internal resistance.[59] Therefore, successful achievement of uniform and thin coating of solid-state electrolytes in 3D architecture will allow for significantly reduced ionic conductivity to be a tolerable consequence.[42]

The capability of the ALD process to achieve the above goal is demonstrated by depositing 100-cycle $Li_{5.1}TaO_z$ thin film on an AAO template with aspect ratio of ~300, as shown in Figure 7. Top-view images in Figure 7a,b indicate that the $Li_{5.1}TaO_z$

dx.doi.org/10.1021/jp4063302 | J. Phys. Chem. C 2013, 117, 20260–20267

thin film is uniformly and conformally coated around the pores of the AAO template. Furthermore, cross-section examination, as seen in Figure 7c,d, shows that the inner surface of the pores is covered by a tubular thin film of $Li_{5.1}TaO_z$. The thickness of the $Li_{5.1}TaO_z$ thin film is measured as ~50 nm from the top (Figure 7b) and the side (Figure 7d). The BSE images in Figure 7 clearly illustrate that the ALD process developed herein is capable of depositing desirable lithium tantalate thin films in high-aspect-ratio substrates, as required in 3D microbatteries.

4. CONCLUSION

Lithium tantalate thin films have been deposited by means of ALD through combining subcycles of Li_2O (LiO^tBu-H_2O) and Ta_2O_5 ($Ta(OEt)_5-H_2O$). All lithium tantalate thin films were deposited at 225 °C, and they were amorphous at as-deposited state. The growth of the lithium tantalate thin films by ALD was proven to be a self-limiting process. Composition (Li/Ta ratio) of the lithium tantalate thin films was controlled by changing the subcycle ratios of Li_2O to Ta_2O_5 (1 to 1, 1 to 6, and 1 to 10). Both XPS and XANES analysis confirmed that Ta in the lithium tantalate thin films had similar chemical environment as that in reference $LiTaO_3$. The as-grown lithium tantalate thin film using 1 Li_2O and 6 Ta_2O_5 subcycles exhibited a lithium-ion conductivity of 2×10^{-8} S/cm at room temperature. Moreover, the ALD process developed in this work successfully deposited lithium tantalate thin films with excellent uniformity and conformality in a 3D AAO template with an aspect ratio of ~300. Given the aforementioned unique advantages, the lithium tantalate thin films prepared by ALD might find potential applications as solid-state electrolytes in 3D lithium-ion microbatteries, which is very promising power supply system for next-generation microelectronic devices.

■ ASSOCIATED CONTENT

Supporting Information

Low-magnification SEM images of the lithium tantalate thin film deposited using pulsing sequence of $1 \times Li_2O + 6 \times Ta_2O_5$ with different ALD cycles; XRD pattern of 400-cycle lithium tantalate thin film deposited using pulsing sequence of $1 \times Li_2O + 6 \times Ta_2O_5$ on the glass substrate; deconvolution of C 1s/4 spectrum of the lithium tantalate thin films deposited using different pulsing sequences; elemental compositions of lithium tantalate thin films deposited using different pulsing sequences as measured by XPS. This material is available free of charge via the Internet at http://pubs.acs.org.

■ AUTHOR INFORMATION

Corresponding Author

*Tel + 1 519 661 2111 x87759; fax + 1 519 661 3020; e-mail xsun@eng.uwo.ca (X.S.).

Notes

The authors declare no competing financial interest.

■ ACKNOWLEDGMENTS

This work was supported by General Motors of Canada, Natural Sciences and Engineering Research Council of Canada (NSERC), Canada Fundation for Innovation (CFI), Ontario Research Fund (ORF), Canadian Light Source (CLS) at University of Saskatchewan, and University of Western Ontario.

■ REFERENCES

(1) Long, J. W.; Dunn, B.; Rolison, D. R.; White, H. S. Three-Dimensional Battery Architectures. *Chem. Rev.* **2004**, *104*, 4463−2292.
(2) Roberts, M.; Johns, P.; Owen, J.; Brandell, D.; Edstrom, K.; Enany, G. E.; Guery, C.; Golodnitsky, D.; Lacey, M.; Lecoeur, C.; et al. 3D Lithium Ion Batteries−from Fundamentals to Fabrication. *J. Mater. Chem.* **2011**, *21*, 9876−9890.
(3) Oudenhoven, J. F. M.; Baggetto, L.; Notten, P. H. L. All-Solid-State Lithium-Ion Microbatteries: a Review of Various Three-Dimensional Concepts. *Adv. Energy Mater.* **2011**, *1*, 10−33.
(4) Bates, J. B.; Dudney, N. J.; Neudecker, B.; Ueda, A.; Evans, C. D. Thin-Film Lithium and Lithium-Ion Batteries. *Solid State Ionics* **2000**, *135*, 33−45.
(5) Souquet, J. L.; Duclot, M. Thin Film Lithium Batteries. *Solid State Ionics* **2002**, *148*, 375−379.
(6) Arthur, T. S.; Bates, D. J.; Cirigliano, N.; Jhonson, D. C.; Malati, P.; Mosby, J. M.; Perre, E.; Rawls, M. T.; Prieto, A. L.; Dunn, B. Three-Dimensional Electrodes and Battery Architectures. *MRS Bull.* **2011**, *36*, 523−531.
(7) Notten, P. H. L.; Roozeboom, F.; Niessen, R. A. H.; Baggetto, L. 3-D Integrated All-Solid-State Rechargeable Batteries. *Adv. Mater.* **2007**, *19*, 4564−4567.
(8) Dunn, B.; Long, J. W.; Rolison, D. R. Rethinking Multifunction in Three Dimensions for Miniaturizing Electrical Energy Storage. *Electrochem. Soc. Interface* **2008**, *17*, 49−53.
(9) Golodnitsky, D.; Nathan, M.; Yufit, V.; Strauss, E.; Freedman, K.; Burstein, L.; Gladkich, A.; Peled, E. Progress in Three-Dimensional (3D) Li-Ion Microbatteries. *Solid State Ionics* **2006**, *177*, 2811−2819.
(10) Rolison, D. R.; Long, J. W.; Lytle, J. C.; Fischer, A. E.; Rhodes, C. P.; Mcevoy, T. M.; Bourg, M. E.; Lubers, A. M. Multifunctional 3D Nanoarchitectures for Energy Storage and Conversion. *Chem. Soc. Rev.* **2009**, *38*, 226−252.
(11) Bae, C.; Shin, H.; Nielsch, K. Surface Modification and Fabrication of 3D Nanostructures by Atomic Layer Deposition. *MRS Bull.* **2011**, *36*, 887−897.
(12) George, S. M. Atomic Layer Deposition: an Overview. *Chem. Rev.* **2010**, *110*, 111−131.
(13) Puurunen, R. L. Surface Chemistry of Atomic Layer Deposition: a Case Study for the Trimethylaluminum/Water Process. *J. Appl. Phys.* **2005**, *97*, 121301.
(14) Elam, J. W.; Routkevitch, D.; Mardilovich, P. P.; George, S. M. Conformal Coating on Ultrahigh-Aspect-Ratio Nanopores of Anodic Alumina by Atomic Layer Deposition. *Chem. Mater.* **2003**, *15*, 3507−3517.
(15) Cheah, S. K.; Perre, E.; Rooth, M.; Fondell, M.; Hårsta, A.; Nyholm, L.; Boman, M.; Gustafsson, T.; Lu, J.; Simon, P.; et al. Self-Supported Three-Dimensional Nanoelectrodes for Microbattery Applications. *Nano Lett.* **2009**, *9*, 3230−3233.
(16) Gerasopoulos, K.; Chen, X.; Culver, J.; Wang, C.; Ghodssi, R. Self-Assembled Ni/TiO_2 Nanocomposite Anode Synthesized *via* Electroless Plating and Atomic Layer Deposition on Biological Scaffolds. *Chem. Commun.* **2010**, *46*, 7349−7351.
(17) Gerasopoulos, K.; Pomerantseva, E.; McCarthy, M.; Brown, A.; Wang, C.; Culver, J.; Ghodssi, R. Hierarchical Three-Dimensional Microbattery Electrodes Combining Bottom-Up Self-Assembly and Top-Down Micromachining. *ACS Nano* **2012**, *6*, 6422−6432.
(18) Li, X.; Meng, X.; Liu, J.; Geng, D.; Zhang, Y.; Banis, M. N.; Li, Y.; Yang, J.; Li, R.; Sun, X.; et al. Tin Oxide with Controlled Morphology and Crystallinity by Atomic Layer Deposition onto Graphene Nanosheets for Enhanced Lithium Storage. *Adv. Funct. Mater.* **2012**, *22*, 1647−1654.
(19) Chen, X.; Pomerantseva, E.; Banerjee, P.; Gregorczyk, K.; Ghodssi, R.; Rubloff, G. Ozone-Based Atomic Layer Deposition of Crystalline V_2O_5 for High Performance Electrochemical Energy Storage. *Chem. Mater.* **2012**, *24*, 1255−1261.
(20) Meng, X.; Liu, J.; Li, X.; Banis, M. N.; Yang, J.; Li, R.; Sun, X. Atomic Layer Deposited $Li_4Ti_5O_{12}$ on Nitrogen-Doped Carbon Nanotubes. *RSC Adv.* **2013**, *3*, 7285−7288.

(21) Kim, S. W.; Han, T. H.; Kim, J.; Gwon, H.; Moon, H. S.; Kang, S. W.; Kim, S. O.; Kang, K. Fabrication and Electrochemical Characterization of TiO_2 Three-Dimensional Nanonetwork Based on Peptide Assembly. *ACS Nano* **2009**, *3*, 1085−1090.
(22) Meng, X.; Zhong, Y.; Sun, Y.; Banis, M. N.; Li, R.; Sun, X. Nitrogen-Doped Carbon Nanotubes Coated by Atomic Layer Deposited SnO_2 with Controlled Morphology and Phase. *Carbon* **2011**, *49*, 1133−1144.
(23) Scott, I. D.; Jung, Y. S.; Cavanagh, A. S.; Yan, Y.; Dillon, A. C.; George, S. M.; Lee, S.-H. Ultrathin Coatings on Nano-$LiCoO_2$ for Li-Ion Vehicular Applications. *Nano Lett.* **2011**, *11*, 414−418.
(24) Guan, D.; Jeevarajan, J. A.; Wang, Y. Enhanced Cycleability of $LiMn_2O_4$ Cathodes by Atomic Layer Deposition of Nanosized-Thin Al_2O_3 Coatings. *Nanoscale* **2011**, *3*, 1465−1469.
(25) Zhao, J.; Qu, G.; Flake, J. C.; Wang, Y. Low Temperature Preparation of Crystalline ZrO_2 Coatings for Improved Elevated-Temperature Performance of Li-Ion Battery Cathodes. *Chem. Commun.* **2012**, *48*, 8108−8110.
(26) Jung, Y. S.; Cavanagh, A. S.; Riely, L. A.; Kang, S.-H.; Dillon, A. C.; Groner, M. D.; George, S. M.; Lee, S.-H. Ultrathin Direct Atomic Layer Deposition on Composite Electrodes for Highly Durable and Safety Li-Ion Batteries. *Adv. Mater.* **2010**, *22*, 2172−2176.
(27) Zhao, J.; Wang, Y. Ultrathin Surface Coatings for Improved Electrochemical Performance of Lithium Ion Battery Electrodes at Elevated Temperature. *J. Phys. Chem. C* **2012**, *116*, 11867−11876.
(28) Ann, D.; Xiao, X. Extended Lithium Titanate Cycling Potential Window with Near Zero Capacity Loss. *Electrochem. Commun.* **2011**, *13*, 796−799.
(29) Liu, J.; Li, X.; Cai, M.; Li, R.; Sun, X. Ultrathin Atomic Layer Deposited ZrO_2 Coating to Enhance the Electrochemical Performance of $Li_4Ti_5O_{12}$ as an Anode Material. *Electrochim. Acta* **2013**, *93*, 195−201.
(30) H, Y.; Yu, X.; Wang, Y.; Li, H.; Huang. Alumina-Coated Patterned Amorphous Silicon as the Anode for a Lithium-Ion Battery with High Coulombic Efficiency. *Adv. Mater.* **2011**, *23*, 4938−4941.
(31) Xiao, X.; Lu, P.; Ahn, D. Ultrathin Multifunctional Oxide Coatings for Lithium Ion Batteries. *Adv. Mater.* **2011**, *23*, 3911−3915.
(32) Riely, L. A.; Cavanagh, A. S.; George, S. M.; Jung, Y. S.; Yan, Y.; Lee, S.-H.; Dillon, A. C. Conformal Surface Coatings to Enhance High Volume Expansion Li-Ion Anode Materials. *ChemPhysChem* **2010**, *11*, 2124−2130.
(33) Meng, X.; Yang, X.-Q.; Sun, X. Emerging Applications of Atomic Layer Deposition for Lithium-Ion Battery Studies. *Adv. Mater.* **2012**, *24*, 3589−3615.
(34) Knoops, H. C. M.; Donders, M. E.; van de Sanden, M. C. M.; Notten, P. H. L.; Kessels, W. M. M. Atomic Layer Deposition for Nanostructured Li-Ion Batteries. *J. Vac. Sci. Technol., A* **2012**, *30*, 010801.
(35) Putkonen, M.; Aaltonen, T.; Alnes, M.; Sajavaara, T.; Nilsen, O.; Fjellvåg, H. Atomic Layer Deposition of Lithium Containing Thin Films. *J. Mater. Chem.* **2009**, *19*, 8767−8771.
(36) Aaltonen, T.; Alnes, M.; Nilsen, O.; Costelle, L.; Fjellvåg, H. Lanthanum Titanate and Lithium Lanthanum Titanate Thin Films Grown by Atomic Layer Deposition. *J. Mater. Chem.* **2010**, *20*, 2877−2881.
(37) Aaltonen, T.; Nilsen, O.; Magrasó, A.; Fjellvåg, H. Atomic Layer Deposition of Li_2O-Al_2O_3 Thin Films. *Chem. Mater.* **2011**, *23*, 4669−4675.
(38) Hämäläinen, J.; Holopainen, J.; Munnik, F.; Hatanpää, T.; Heikkilä, M.; Ritala, M.; Leskelä, M. Lithium Phosphate Thin Films Grown by Atomic Layer Deposition. *J. Electrochem. Soc.* **2012**, *159*, A259−A263.
(39) Hämäläinen, J.; Munnik, F.; Hatanpää, T.; Holopainen, J.; Ritala, M.; Leskelä, M. Study of Amorphous Lithium Silicate Thin Films Grown by Atomic Layer Deposition. *J. Vac. Sci. Technol., A* **2012**, *30*, 01A106.
(40) Østreng, E.; Vajeeston, P.; Nilsen, O.; Fjellvåg, H. Atomic Layer Deposition of Lithium Nitride and Carbonate Using Lithium Silylamide. *RSC Adv.* **2012**, *2*, 6315−6322.
(41) Comstock, D. J.; Elam, J. W. Mechanistic Study of Lithium Aluminum Oxide Atomic Layer Deposition. *J. Phys. Chem. C* **2013**, *117*, 1677−1683.
(42) Glass, A. M.; Nassau, K.; Negran, T. J. Ionic Conductivity of Quenched Alkali Niobate and Tantalate Glasses. *J. Appl. Phys.* **1978**, *49*, 4808−4811.
(43) Li, Z.; Chen, X.; Hu, X. The Preparation of Ionic Conductance of Nano-Amorphous Li_xTaO_y Thin Film. *J. Phys. D: Appl. Phys.* **1996**, *29*, 2740−2744.
(44) Kukli, K.; Ritala, M.; Leskelä, M. Atomic Layer Epitaxy Growth of Tantalum Oxide Thin Films from $Ta(OC_2H_5)_5$ and H_2O. *J. Electrochem. Soc.* **1995**, *142*, 1670−1675.
(45) Cavanagh, A. S.; Lee, Y.; Yoon, B.; George, S. M. Atomic Layer Deposition of LiOH and Li_2CO_3 Using Lithium t-Butoxide as the Lithium Source. *ECS Trans.* **2010**, *33*, 223−229.
(46) Kukli, K.; Aarik, J.; Aidla, A.; Siimon, H.; Ritala, M.; Leskelä, M. In Situ Study of Atomic Layer Epitaxy Growth of Tantalum Oxide Thin Films from $Ta(OC_2H_5)_5$ and H_2O. *Appl. Surf. Sci.* **1997**, *112*, 236−242.
(47) Nilsen, O.; Rauwel, E.; Fjellvåg, H.; Kjekshus, A. Growth of $La_{1-x}Ca_xMnO_3$ Thin Films by Atomic Layer Deposition. *J. Mater. Chem.* **2007**, *17*, 1466−1475.
(48) Gaultois, M. W.; Grosvenor, A. P. XANES and XPS Investigations of the Local Structure and Final-State Effects in Amorphous Metal Silicates: $(ZrO_2)_x(TiO_2)_y(SiO_2)_{1-x-y}$. *Phys. Chem. Chem. Phys.* **2012**, *14*, 205−217.
(49) Yang, S.; Wang, D.; Liang, G.; Yiu, Y. M.; Wang, J.; Liu, L.; Sun, X.; Sham, T.-K. Soft X-Ray XANES Studies of Various Phases Related to $LiFePO_4$ Based Cathode Materials. *Energy Environ. Sci.* **2012**, *5*, 7007−7016.
(50) Kim, T. W.; Hur, S. G.; Han, A. R.; Hwang, S.-J.; Choy, J.-H. Effect of Bond Covalency on the Lattice Stability and Fatigue Behavior of Ferroelectric Bismuth Transition-Metal Oxides. *J. Phys. Chem. C* **2008**, *112*, 3434−3438.
(51) Hu, Y. F.; Xu, R. K.; Dynes, J. J.; Blyth, R. I. R.; Yu, G.; Kozak, L. M.; Huang, P. M. Coordination Nature of Aluminum (Oxy)hydroxides Formed Under the Influence of Tannic Acid Studied by X-Ray Absorption Spectroscopy. *Geochim. Cosmochim. Acta* **2008**, *72*, 1959−1969.
(52) Liu, J.; Tang, Y.; Xiao, B.; Sham, T.-K.; Li, R.; Sun, X. Atomic Layer Deposited Aluminum Phosphate Thin Films on N-Doped CNTs. *RSC Adv.* **2013**, *3*, 4492−4495.
(53) Gitmans, F.; Sitar, Z.; Günter, P. Growth of Tantalum Oxide and Lithium Tantalate Thin Films by Molecular Beam Epitaxy. *Vacuum* **1995**, *46*, 939−942.
(54) Atanassova, E.; Tyuliev, G.; Paskaleva, A.; Spassov, D.; Kostov, K. XPS Study of N_2 Annealing Effect on Thermal Ta_2O_5 Layers on Si. *Appl. Surf. Sci.* **2004**, *225*, 86−99.
(55) Miikkulainen, V.; Nilsen, O.; Laitinen, M.; Sajavaara, T.; Fjellvåg, H. Atomic Layer Deposition of $Li_xTi_yO_z$ Thin Films. *RSC Adv.* **2013**, *3*, 7537−7542.
(56) Glass, A. M.; Nassau, K. Lithium Ion Conduction in Rapidly Quenched Li_2O-Al_2O_3, Li_2O-Ga_2O_3, and Li_2O-Bi_2O_3 Glasses. *J. Appl. Phys.* **1980**, *51*, 3756−3761.
(57) Huanosta, A.; West, A. R. The Electrical Properties of Ferroelectric $LiTaO_3$ and Its Solid Solutions. *J. Appl. Phys.* **1987**, *61*, 5386−5391.
(58) Murugan, R.; Thangadurai, V.; Weppner, W. Fast Lithium Ion Conduction in Garnet-Type $Li_7La_3Zr_2O_{12}$. *Angew. Chem. Int. Ed.* **2007**, *46*, 7778−7781.
(59) Goodenough, J. B. Solid Electrolytes. *Pure Appl. Chem.* **1995**, *67*, 931−938.
(60) West, A. R. Solid Electrolytes. *Ber. Bunsenges. Phys. Chem.* **1989**, *93*, 1235−1241.
(61) Takada, K. Progress and Prospective of Solid-State Lithium Batteries. *Acta Mater.* **2013**, *61*, 759−770.
(62) Thangadurai, V.; Weppner, W. Recent Progress in Solid Oxide and Lithium Ion Conducting Electrolytes Research. *Ionics* **2006**, *12*, 81−92.